

Electronic Supplementary Information (ESI) for:

Using iron sulphate to form both n-type and p-type *pseudo*-  
thermoelectrics: Non-hazardous and ‘second life’  
thermogalvanic cells

Mark A. Buckingham,<sup>a</sup> Kristine Laws,<sup>a</sup> Jason T. Sengel<sup>a</sup> and Leigh Aldous<sup>a,\*</sup>

<sup>a</sup> Department of Chemistry, Britannia House, King’s College London, London,  
SE1 1DB, UK

\* Corresponding author: [leigh.aldous@kcl.ac.uk](mailto:leigh.aldous@kcl.ac.uk)

## Contents

**Table S1:** Tabulated data to calculate potential HCN evolution from reported in-series thermocell systems and maximum power produced by devices

**Figure S1:** Optimisation of the  $\text{FeSO}_4$  and  $\text{FeSO}_4 + [\text{HSO}_4]^-$  n-type thermocells

**Figure S2:** Temperature dependence on  $aS_e$  (altering  $T_h$ )

**Figure S3:** IR spectra of iron-free  $[\text{HSO}_4]^-$  and  $[\text{SO}_4]^{2-}$

**Table S2:** Tabulated values for the Thermoelectrochemical speciation model

**Figure S4:** Thermoelectrochemical speciation; effect of varying ionic radius

**Figure S5:** Scan rate study of  $\text{FeSO}_4$ ,  $\text{Fe}(\text{HSO}_4)$  and  $\text{Fe}(\text{SO}_4)_2$ .

**Table S3:** Cyclic voltammetric table of data

**Figure S6:** Cold vs hot  $R_{\text{ET}}$  comparison and gold vs graphite comparison

**Figure S7:** Nyquist plots for gold and graphite electrode thermocell systems

**Figure S8:** Nyquist plots and fitting for gold vs graphite electrode thermocell systems

**Figure S9:** Nyquist plots and fitting for hot vs cold working electrode impedance measurements

**Figure S10:** Cyclic voltammetric data including the mixed thermocell system

**Figure S11:** Electrochemical impedance and thermocell resistances including the mixed system

**Figure S12:** Thermoelectrochemical data Figure 1 & 2 including the mixed thermocell system

## Tabulated values for HCN evolution calculation and maximum power produced by devices

**Table S1** – Experimental details and calculations of potential HCN evolved from  $[\text{Fe}(\text{CN})_6]^{4-}$  used in in-series thermocell devices (used to prepare Table 1).

Corresponding author / Reference	Thermocell dimensions area (cm <sup>2</sup> )   height (cm)	Thermocell volume / cm <sup>3</sup>	Total thermocells   total half-cells	Total volume / cm <sup>3</sup>	$[\text{Fe}(\text{CN})_6]^{4-}$ conc. / M	Potential HCN from $[\text{Fe}(\text{CN})_6]^{4-}$ / mg	Applied $\Delta T^*$ / K	$V_{\text{OCP}}$ / V	Maximum power produced by device / $\mu\text{W}$
Zhou (2016) <sup>2</sup>	0.07   0.1	0.007	118   59	0.42	0.1	6.8	27	<i>ca.</i> 0.7	0.3 <sup>a</sup>
Kang (2019) <sup>4</sup>	1   0.26	0.26	2   1	0.26	0.2	8.4	20	0.074	0.9 <sup>b</sup>
Aldous (2016) <sup>1</sup>	2.0   0.25	0.50	4   2 <sup>#</sup>	1	0.1	16.3	50	0.043	5.4 <sup>c</sup>
Baughman (2017) <sup>3</sup>	1   0.26	0.26	112   56	14.56	0.2	472.2	39	2.182	n/a <sup>d</sup>
Lee (2020) <sup>5</sup>	0.78   0.12	0.94	64   32	29.95	0.45	2185.5	25	2.05	2500 <sup>e</sup>

<sup>#</sup> Unlike the other devices, this device was two in-series pairs connected in-parallel, to double both voltage and current.

<sup>\*</sup> These are the reported applied  $\Delta T$  values; in most cases the real  $\Delta T$  values experienced across the electrodes in the devices were smaller.

<sup>a</sup> Reported value.

<sup>b</sup> Calculated based upon device reported to produce 266.5% of the power of the weaker cell (472.9 mWm<sup>-2</sup>; electrode surface area of 1 cm<sup>2</sup>).

<sup>c</sup> Calculated using the reported  $V_{\text{OCP}}$  and  $j_{\text{sc}} = 631 \text{ mA m}^{-2}$ , and electrode surface area of 8 cm<sup>2</sup>.

<sup>d</sup> Only  $V_{\text{OCP}}$  reported for complete device.

<sup>e</sup> Calculated using reported  $V_{\text{OCP}}$  and reported  $P_{\text{max}} = 0.5 \text{ W m}^{-2}$ , and electrode surface area of 49.92 cm<sup>2</sup>.

The relevant electrode surface areas, cell volumes, *etc.* were based upon the following details taken directly from the relevant sections of the manuscripts:

<b>Notes on each thermocell design</b>	
Zhou (2016) <sup>2</sup>	“an integrated device containing 59 PFC and 59 PPF gel units (1 mm in height and 3 mm in diameter), with bridging Au/Cr inter-connections on flexible PI substrate”; cells appeared cylindrical in schematics.
Kang (2019) <sup>4</sup>	Thermocell details are largely absent, but there is a small note on the electrode materials “The carbon electrodes were cut into 1 cm × 1 cm squares and assembled into the thermocell evaluation device” The thermocell itself appears to be the same as that previously reported by Baughman <i>et al.</i> <sup>3</sup>
Aldous (2016) <sup>1</sup>	“Stainless steel 304 CR2032 battery button cells and their platinum-coated analogues were crimped using a hydraulic press, and thus measurements were made in hermitically sealed casings”; the internal cavity of the CR2032 casing is <i>ca.</i> 1 cm <sup>3</sup>
Baughman (2017) <sup>3</sup>	“thermocell structure, which consists of two Ti current collectors, two thermocell electrodes, a thermal separator attached to the cold-side thermocell electrode, a 2.6 mm thick plate spacer made of polyether ether ketone that defines the electrolyte volume at cell centre, and two rubber O-rings. The carbon electrodes are 1 cm <sup>2</sup> in area.”
Lee (2020) <sup>5</sup>	“Graphite foil (35 mm thick) was used as electrode material for a TEC module consisting of 64 unit cells. The distance between the two electrodes and the electrode area were 1.2 cm and 0.78 cm <sup>2</sup> , respectively”

## Concentration study of the $[\text{Fe}(\text{SO}_4)]^{0/+}$ and $[\text{Fe}(\text{HSO}_4)]^{+/2+}$ *n*-type thermocells

The  $[\text{Fe}(\text{SO}_4)]^{0/+}$  *n*-type thermocell has already been previously reported, both in the presence and absence of acid.<sup>1,6</sup> Here we investigated the effect of increasing concentration of  $\text{FeSO}_4$  (equimolar ratios of  $\text{Fe}(\text{II})\text{SO}_4$  and  $\text{Fe}(\text{III})\text{SO}_4$ ; Figure S1(a-c)), along with the effect of various concentrations of  $\text{NaHSO}_4$  (the  $[\text{Fe}(\text{HSO}_4)]^{+/2+}$  *n*-type thermocell; Figure S1(d-f)). Increasing the concentration of  $\text{FeSO}_4$  had no significant effect upon the Seebeck coefficient of the system (Figure S1(a)), but increased both the short circuit current density and maximum power density of the system up to 0.75 M of each (Figure S1(b & c)); these decreased at the highest concentration investigated (1 M of both  $\text{Fe}(\text{II})\text{SO}_4$  and  $\text{Fe}(\text{III})\text{SO}_4$ ), which matches what has been previously observed for the  $\text{FeClO}_4$  system.<sup>4</sup> Addition of  $[\text{HSO}_4]^-$  (as  $\text{NaHSO}_4$ ) increased the Seebeck of the thermocell, due to a decrease in pH, as discussed in the main manuscript. While the addition of 0.5 M  $\text{NaHSO}_4$  increased the short circuit current density and maximum power density, there was no significant difference between the range of 0.5 M and 1.5 M  $\text{NaHSO}_4$ .

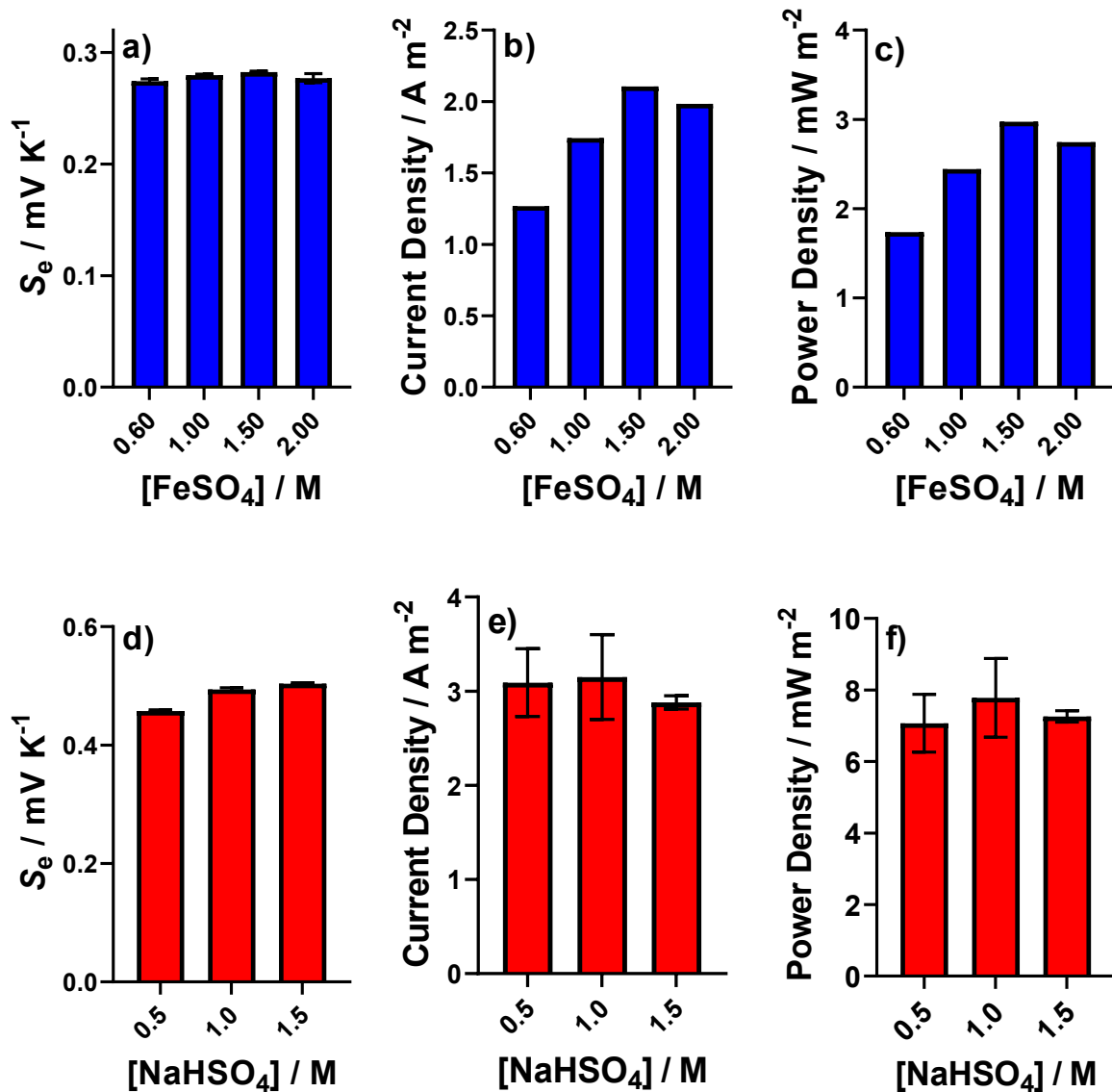


**Figure S1** – Bar graph for (a-c) the  $[\text{Fe}(\text{SO}_4)]^{0/+}$  thermocell system and (d-f) the  $[\text{Fe}(\text{HSO}_4)]^{+/2+}$  thermocell system. Displaying the measured Seebeck coefficient  $S_e$  (a & d), short-circuit current density ( $j_{\text{sc}}$ ) and (c & f) maximum power output ( $P_{\text{max}}$ ) at various concentrations of either equimolar Fe(II)SO<sub>4</sub> and Fe(III)SO<sub>4</sub> (a-c; x-axis is the sum, e.g. 0.60 = 0.30 M Fe(II)SO<sub>4</sub> and 0.30 M Fe(III)SO<sub>4</sub>) or for a fixed concentration of 0.3 M Fe(II)SO<sub>4</sub> and 0.3 M Fe(III)SO<sub>4</sub> with various concentrations of NaHSO<sub>4</sub> (d-f). All measured using an applied  $\Delta T = 20 \text{ K}$  and  $T_c = 20^\circ\text{C}$ .

## Temperature dependence on $aS_e$ (altering $T_h$ )

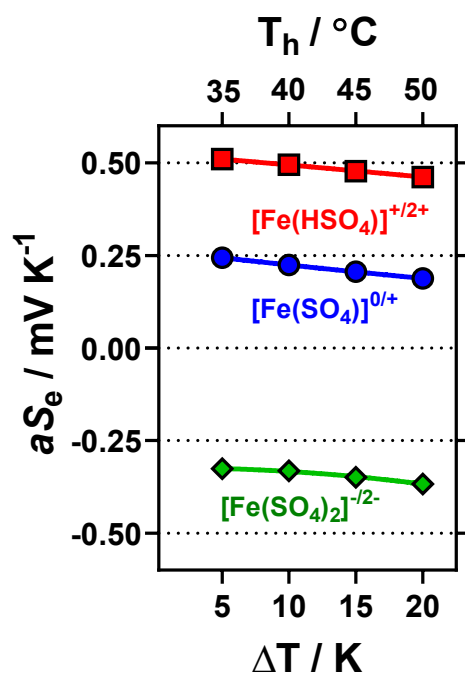


**Figure S2** - Plot of the  $aS_e$  measured at four different  $\Delta T$  values for 0.3 M Fe(II) and 0.3 M Fe(III) sulphate ( $[\text{Fe}(\text{SO}_4)]^{0/+}$ ), and the same system but also containing 1.5 M  $\text{NaHSO}_4$  ( $[\text{Fe}(\text{HSO}_4)]^{+/2+}$ ) or 1.5 M  $\text{Na}_2\text{SO}_4$  ( $[\text{Fe}(\text{SO}_4)_2]^{-/2-}$ ). The  $aS_e$  corresponded to the measured  $\Delta V$  and divided by the applied  $\Delta T$ ; the  $\Delta T$  was controlled by fixing  $T_c = 30^\circ\text{C}$ , and varying the applied  $T_h$  between  $35^\circ\text{C}$  and  $50^\circ\text{C}$ . The polynomial lines of best fit have been added to guide the eye of the reader and are not intended to model the data.

## IR spectra of iron-free NaHSO<sub>4</sub> and Na<sub>2</sub>SO<sub>4</sub> solutions

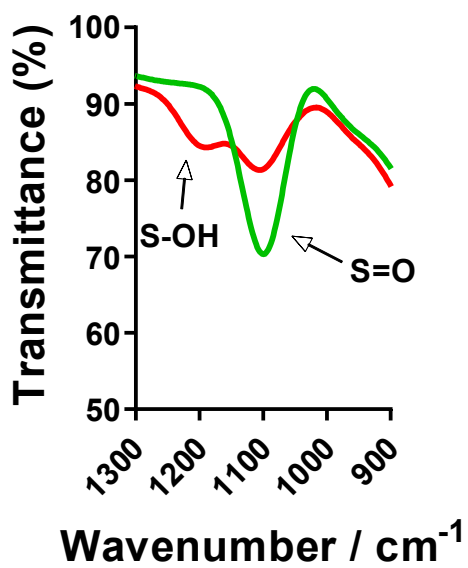


**Figure S3** – IR spectra of 0.075 M Na<sub>2</sub>SO<sub>4</sub> (green) and 0.075 M NaHSO<sub>4</sub> (red). NB: These are measured in the absence of iron sulphate.



## Tabulated values for the Thermochemical speciation model

The  $\Delta S_{rc}$  for the various systems had to be calculated. This was done using

$$\frac{\Delta V}{\Delta T} = aS_e = -\frac{\Delta S_{rc}}{nF}$$

However, while the applied value of  $\Delta T$  has been used throughout this manuscript, calibration of our cell using the standard 0.4 M potassium ferri/ferrocyanide system demonstrated that there were heat losses in our cell. This meant that when  $\Delta T = 20$  K was applied, only  $\Delta T = 18$  K was experienced at the electrodes (see reference<sup>7</sup> for full details). Therefore  $\Delta V$  values were obtained experimentally and were used to calculate the  $\Delta S_{rc}$  values using  $\Delta T = 18$  K. These corresponded to the  $aS_e$  values for  $[\text{Fe}(\text{SO}_4)_2]^{-/2-}$  and  $[\text{Fe}(\text{HSO}_4)]^{+/2+}$  shown in Figure 1 (+0.27 mV K<sup>-1</sup> and +0.50 mV K<sup>-1</sup>, respectively); for  $[\text{Fe}(\text{SO}_4)_2]^{-/2-}$  the largest  $aS_e$  value from Figure 3 (-0.4 mV K<sup>-1</sup>) was used. The  $\Delta S_{rc}$  values were calculated for these systems, and these are summarised in Table S2 (vs literature analogues).

**Table S2** – Table of data for the proposed model speciation displaying the reported of measured  $\Delta S_{rc}$ , ionic radius,  $r$ , proposed  $\Delta z^2$ , and calculated  $(z_{\text{Ox}}^2 - z_{\text{Red}}^2)/r$  for the data shown in Figure 6 & Figure S3.

Fe Species	Ref	$\Delta S_{rc}$	$r / \text{\AA}$	Proposed $\Delta z^2$ ( $z_{\text{Ox}}^2 / z_{\text{Red}}^2$ )	Calculated $(z_{\text{Ox}}^2 - z_{\text{Red}}^2)/r$
$[\text{Fe}(\text{H}_2\text{O})_6]^{3+/2+}$	6	+154	3.3 <sup>8</sup>	5 ( $3^2 - 2^2$ )	1.520
$[\text{Fe}(\text{CN})_6]^{3-/4-}$	9	-135	4.4 <sup>10</sup>	-9 ( $-3^2 - -4^2$ )	-1.590
$[\text{Fe}(\text{HSO}_4)]^{2+/+}$	6	+82	5.1	3 ( $2^2 - 1^2$ )	0.590
“ $[\text{Fe}(\text{SO}_4)]^{0/+}$ ”	*	+29	5.1	1 ( $1^2 - 0^2$ )	
“ $[\text{Fe}(\text{SO}_4)_2]^{-/2-}$ ”	*	-43	5.1	-3 ( $-1^2 - -2^2$ )	
“ $[\text{Fe}(\text{HSO}_4)]^{2+/+}$ ”	*	+54	5.1	n/a (mixed)	

\* This work

## Speciation model with varying $r$ values

Initially, the  $\Delta S_{rc}$  can be determined from the experimentally measured  $S_e$ , where the largest values of  $\Delta S_{rc}$  measured for the “[Fe(SO<sub>4</sub>)]<sup>0/+</sup>”, “[Fe(HSO<sub>4</sub>)]<sup>+/2+</sup>” and “[Fe(SO<sub>4</sub>)<sub>2</sub>]<sup>-/2-</sup>” systems are 30, 59 and -39 J K<sup>-1</sup> mol<sup>-1</sup>, respectively. However, the  $r$  value had to be estimated; this was calculated by estimating that of a Fe(SO<sub>4</sub>) species with a single layer of water of hydration, as shown below;

Bond Length/ Ionic Radius (Å)	Description
1.8	(Fe-O where O is [SO <sub>4</sub> ] <sup>2-</sup> ) <sup>11</sup>
+ 2.05	(Fe-O where O is H <sub>2</sub> O) <sup>12</sup>
+ (2.7-0.6)	(H <sub>2</sub> O diameter <sup>13</sup> – O atomic radius <sup>14</sup> accounted for in bond length)
+ (4.8-0.6)	([SO <sub>4</sub> ] <sup>2-</sup> ionic diameter <sup>12</sup> – O atomic radius <sup>14</sup> accounted for in bond length)
= 10.2 Å	Diameter
= 5.1 Å	Radius

From this a fixed  $r$  value of 5.1 Å was estimated, and this was used to prepare the Figure shown in the main manuscript

To investigate the validity of using this  $r$  value (or the potential implications of using an over- or under-estimated  $r$  value) a comparison was prepared, using  $r$  values of 4 Å and 6 Å (shown in Figure S4). This was done for the [Fe(SO<sub>4</sub>)]<sup>0/+</sup> and [Fe(SO<sub>4</sub>)<sub>2</sub>]<sup>-/2-</sup> redox couples. This shows that the significant changes in the ionic radius has very little effect on the relative position of the [Fe(SO<sub>4</sub>)]<sup>0/+</sup> redox couple. The change in ionic radius had a larger effect upon the [Fe(SO<sub>4</sub>)<sub>2</sub>]<sup>-/2-</sup> redox couple, but it still strongly corresponded with  $(z_{Ox}^2 - z_{Red}^2) = -3$  (both shown as brown circles).

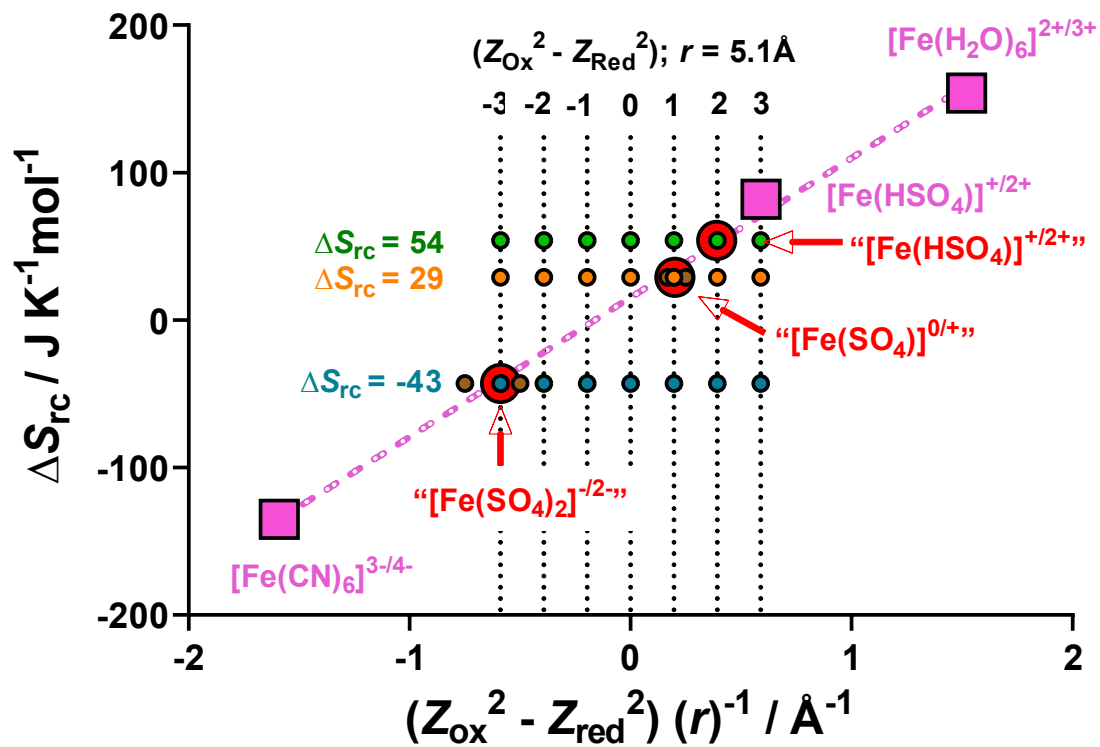


**Figure S4** – Speciation plot repeating what is shown in Figure 4. Shows the calculated  $\Delta S_{rc}$  vs  $(Z_{\text{Ox}}^2 - Z_{\text{Red}}^2)/r$  relationships for the  $[\text{Fe}(\text{SO}_4)]^{0/+}$ ,  $[\text{Fe}(\text{HSO}_4)]^{+2+}$  and  $[\text{Fe}(\text{SO}_4)_2]^{-2-}$  systems investigated here, using  $r$  fixed as 5.1 Å (red circles). The influence of  $r$  is evaluated by plotting the same data but using  $r$  as 4 Å or 6 Å for  $[\text{Fe}(\text{HSO}_4)]^{+2+}$  (blue circles) and  $[\text{Fe}(\text{SO}_4)_2]^{-2-}$  (brown circles); circles closest to 0 on the  $x$ -axis corresponds to the largest  $r$  value. The relatively minor effect of  $r$  (relative to  $Z_{\text{Ox}}^2 - Z_{\text{Red}}^2$ ) is clearly observed.

Scan rate study of the  $[\text{Fe}(\text{SO}_4)]^{0/+}$ ,  $[\text{Fe}(\text{HSO}_4)]^{+/2+}$  and  $[\text{Fe}(\text{SO}_4)_2]^{-/2-}$  systems

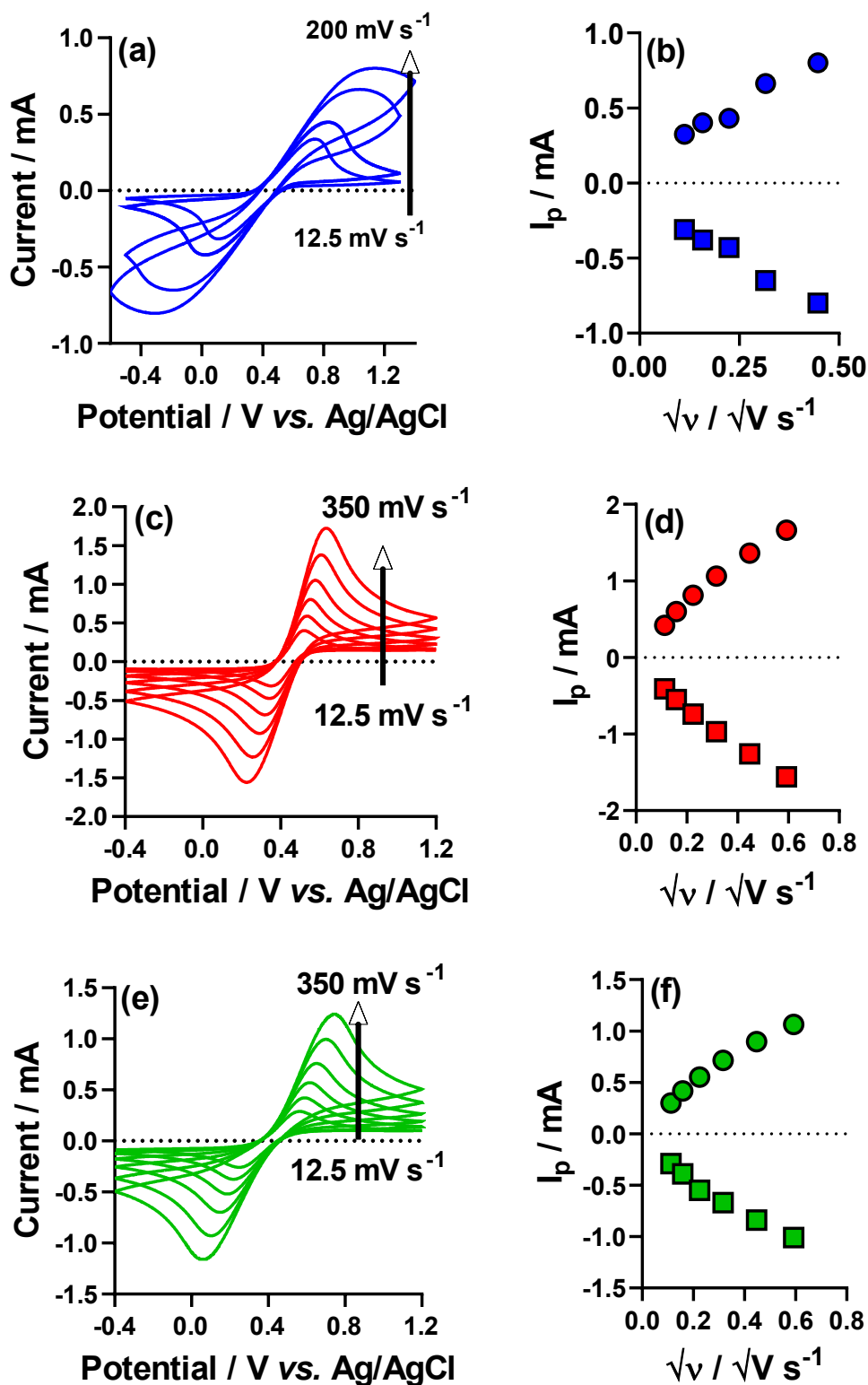


**Figure S5** – Cyclic voltammetric scan rate studies of the three investigated thermocell systems, namely 0.3 M  $\text{Fe}(\text{II})\text{SO}_4$  and 0.3 M  $\text{Fe}(\text{III})\text{SO}_4$  in the (a) absence and presence of either (b) 1.5 M  $\text{Na}_2\text{SO}_4$  or (c) 1.5 M  $\text{NaHSO}_4$ . The voltammograms were measured at a 1.6 mm diameter Au electrode at ambient temperature, between scan rates of 12.5 and 350  $\text{mV s}^{-1}$ . The  $I_p$  vs square

root of scan rate has also been plotted ((b), (d) and (f), respectively), for both the oxidative and reductive peaks.

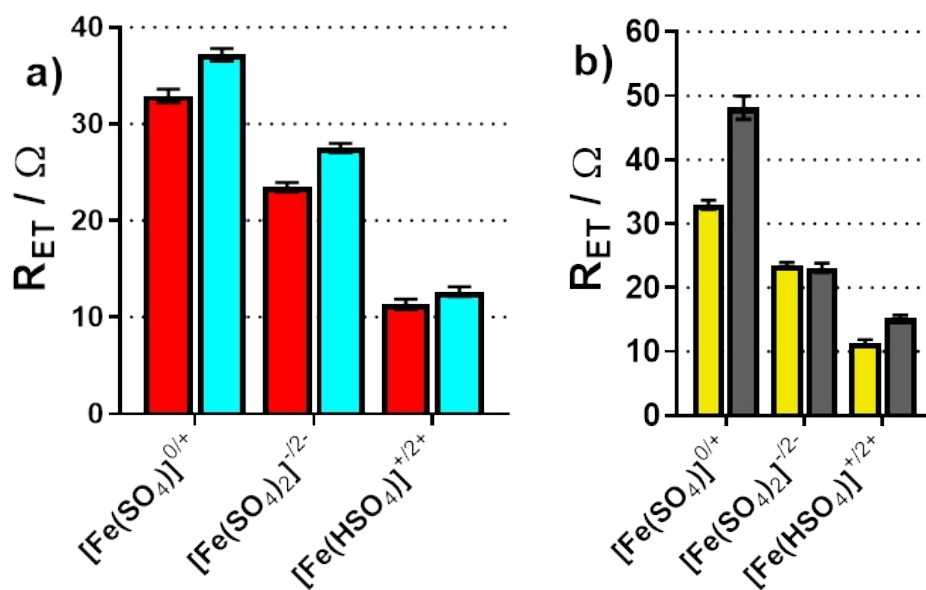
It is important to remember that (a) and (b) cover highly concentrated systems in the complete absence of additional supporting electrolyte; the other systems are also highly concentrated and relatively poorly supported (0.6 M redox-active species to 1.5 M non-redox active additives). Hence all systems (but especially (a) and (b)) likely suffer from a relatively high resistance (*e.g.* IR drop) and electrostatic interactions. Clearly addition of 1.5 M Na<sub>2</sub>SO<sub>4</sub> or NaHSO<sub>4</sub> improves the resolution of the cyclic voltammograms, and appear to suggest improvements in either the kinetics of electron transfer and/or ohmic drop; impedance spectroscopy (discussed later) indicates both. Therefore the slight non-linearity of the  $I_p$  vs  $v^{0.5}$  indicates either quasi-reversible kinetics or non-ideality in the concentrated electrolyte (once again, both are likely contributing factors).

## Cyclic voltammetric table of data

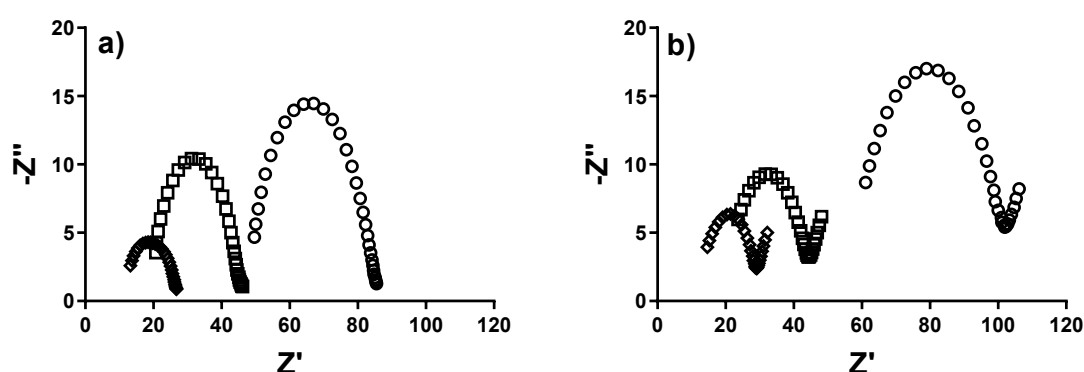
**Table S3** – Tabulated values from the cyclic voltammograms (CVs) shown in Figure 7, for: peak potential of the oxidation peak ( $E_{\text{Ox}}$ ), peak potential of the reduction peak ( $E_{\text{Red}}$ ), half-way point between the two peaks ( $E_{1/2}$ ) and the peak-to-peak separation ( $\Delta E_p$ ). All measured in the absence of supporting electrolyte, and at ambient temperature. The experimental setup comprised of a 1.6 mm diameter Au working electrode, Pt wire counter electrode, and measured vs. Ag/AgCl reference electrode at a scan rate of 100 mVs<sup>-1</sup>.

System	$E_{\text{Ox}} / \text{V}$	$E_{\text{Red}} / \text{V}$	$E_{1/2} / \text{V}$	$\Delta E_p / \text{V}$
<b>[Fe(SO<sub>4</sub>)]<sup>0/+</sup></b>	0.800	0.077	0.438	0.723
<b>[Fe(SO<sub>4</sub>)<sub>2</sub>]<sup>2-/-</sup></b>	0.565	0.233	0.399	0.332
<b>[Fe(HSO<sub>4</sub>)]<sup>2+/+</sup></b>	0.549	0.319	0.434	0.230

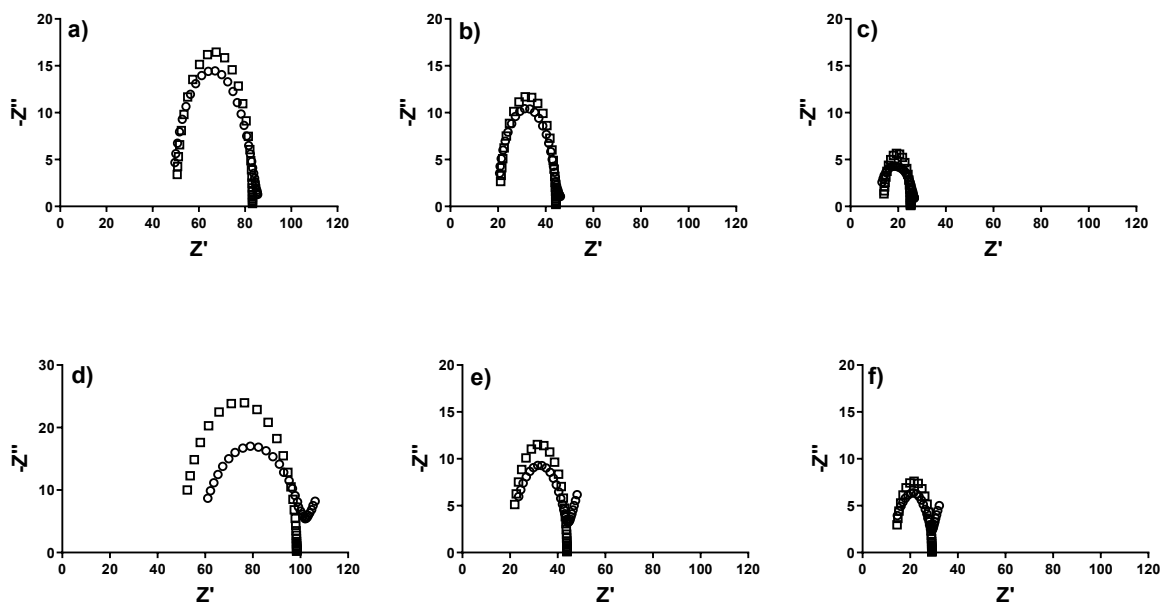
## Electrochemical Impedance Spectroscopy data and Nyquist plots



**Figure S6** – Bar charts plotting the  $R_{ET}$  measured *in situ* in the thermocell for the  $[\text{Fe}(\text{SO}_4)]^{0/+}$ ,  $[\text{Fe}(\text{SO}_4)_2]^{-/2-}$  and  $[\text{Fe}(\text{HSO}_4)]^{+/2+}$  systems. The left bar chart (a) summarises the  $R_{ET}$  when measured at gold electrodes where the working electrode was the hot electrode (red) or the cold electrode (blue). The right bar chart (b) summarises the  $R_{ET}$  when measured at gold electrodes (yellow) and graphite electrodes (grey), where the working electrode was the hot electrode. All  $R_{ET}$  values were determined using the  $R_s$  values shown in Figure 8. The raw and fitted spectra are shown in Figures S7-9; the fitting model has been previously reported.<sup>6</sup>

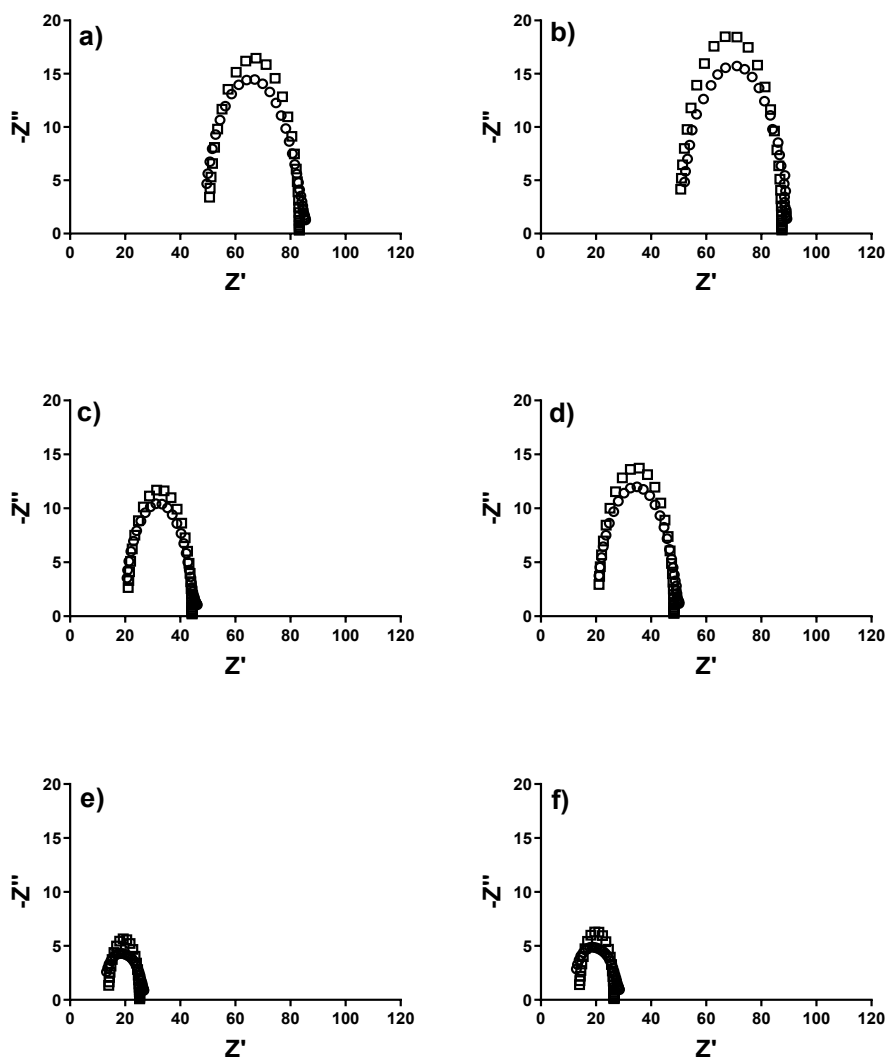


**Figure S7** – Nyquist and fitting plots for the impedance data for the  $[\text{Fe}(\text{SO}_4)]^{0/+}$  (circle),  $[\text{Fe}(\text{SO}_4)_2]^{-/2-}$  (square) and  $[\text{Fe}(\text{HSO}_4)]^{+/2+}$  (diamond) systems, at (a) gold electrodes and (b) graphite electrodes. Fitted spectrums are shown in Figures S8 and S9. All measured *in situ* in the thermogalvanic cell, with  $T_c = 22^\circ\text{C}$  and  $T_h = 40^\circ\text{C}$  (applied  $\Delta T = 18\text{ K}$ ).



**Figure S8** – Nyquist and fitting plots for the impedance data for the  $[\text{Fe}(\text{SO}_4)]^{0/+}$  (a & b),  $[\text{Fe}(\text{SO}_4)_2]^{-/2-}$  (c & d) and  $[\text{Fe}(\text{HSO}_4)]^{+/2+}$  (e & f) systems, where the working electrode was either gold (a-c) or graphite (d-f). All experimental data is shown as circles and all fitting data is shown as squares; the resulting  $R_{\text{ET}}$  values are plotted in Figure S4(b). Experimental conditions as per Figure S7.

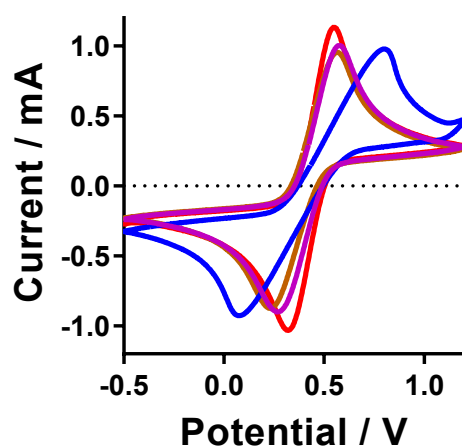




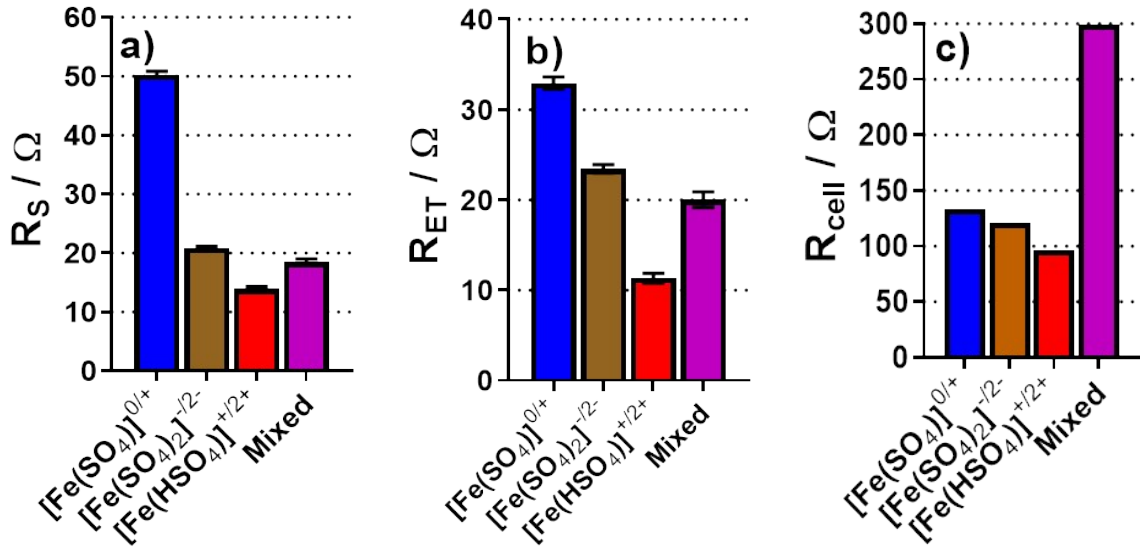
**Figure S9** – Nyquist and fitting plots for the impedance data for the  $[\text{Fe}(\text{SO}_4)]^{0/+}$  (a & b),  $[\text{Fe}(\text{SO}_4)_2]^{-/2-}$  (c & d) and  $[\text{Fe}(\text{HSO}_4)]^{+/2+}$  (e & f) systems, where the working electrode was either the hot (a, c & e) or the cold (b, d & f) electrode. All experimental data is shown as circles and all fitted data shown as squares; the resulting  $R_{\text{ET}}$  values are plotted in Figure S4(a). Experimental conditions as per Figure S7.

## Mixed iron sulphate system analysis

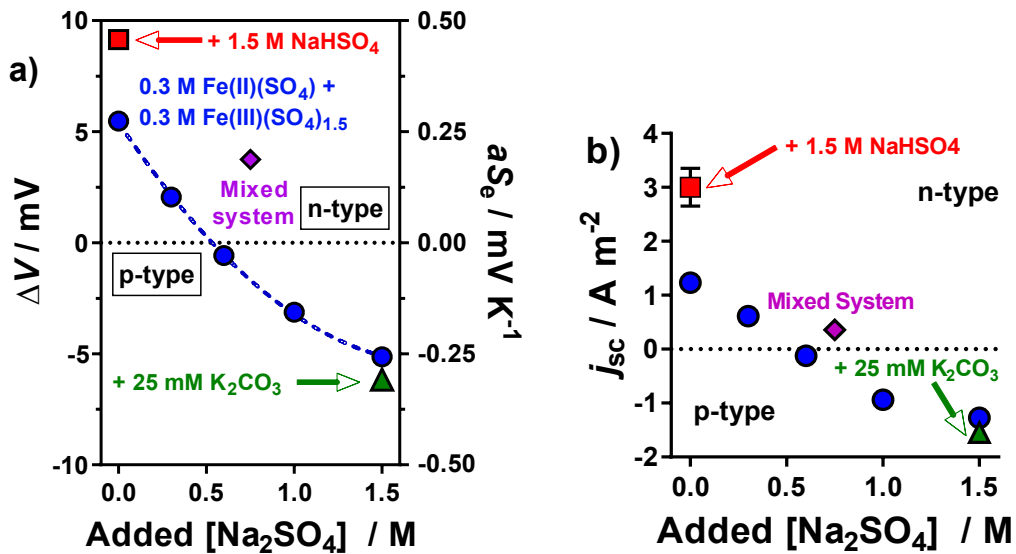
The mixed iron sulphate system (a 50:50 mixture of the  $[\text{Fe}(\text{HSO}_4)]^{+/2+}$  and  $[\text{Fe}(\text{SO}_4)_2]^{-/2-}$  systems) was evaluated, in comparison to the three systems extensively investigated ( $[\text{Fe}(\text{SO}_4)]^{0/+}$ ,  $[\text{Fe}(\text{HSO}_4)]^{+/2+}$  and  $[\text{Fe}(\text{SO}_4)_2]^{-/2-}$ ). This was performed by cyclic voltammetric analysis (Figure S8). The electrochemical impedance analysis for the mixed system matched the general trend in  $R_S$  and  $R_{\text{ET}}$  established by the three other systems (Figure S11, a and b). The  $R_{\text{cell}}$  did not follow this trend, and the mixed cell had a much larger  $R_{\text{cell}}$  value. However the cause of this different is likely due to the smaller driving force in the thermocell due to the lower  $S_e$  value in the mixed system. An additional reason could be due to the presence of thermoelectrochemically inactive species, *e.g.* two distinct species with different  $S_e$  values, with only the species with the larger  $S_e$  value undergoing thermogalvanic chemistry and therefore yielding the observed  $R_{\text{cell}}$  value. Further work is required to quantify the relative contributions of both possibilities. Finally, the fundamental thermogalvanic parameters of the mixed systems are plotted *vs* those of all the other systems investigated here (Figure S12).



**Figure S10** – Cyclic voltammograms (CVs) recorded for the  $[\text{Fe}(\text{SO}_4)]^{0/+}$  (blue),  $[\text{Fe}(\text{SO}_4)_2]^{-/2-}$  (brown) and  $[\text{Fe}(\text{HSO}_4)]^{+/2+}$  (red) and mixed (purple) electrolyte systems. No additional supporting electrolyte was added; CVs were measured using a 3-electrode setup at ambient temperature, using an Au working electrode with a Ag/AgCl reference electrode at a scan rate of  $100 \text{ mV s}^{-1}$ .



**Figure S11** – NB: These are adapted Figure 8, to included the mixed system. Bar charts summarising (a) the solution resistance,  $R_S$  and (b) electron transfer resistance,  $R_{ET}$  for the three systems and mixed system; all quantified using impedance spectroscopy in the non-isothermal thermocell. Also shown is (c) the calculated total thermocell resistance,  $R_{cell}$  of the thermogalvanic cell, based upon Ohm's Law ( $V = IR$ ) from the  $I-V$  plots measured from the thermocell once steady-state discharge has been achieved. All measurements recorded at  $T_c = 22^\circ\text{C}$ ;  $\Delta T = 18\text{ K}$ ), using gold electrodes.



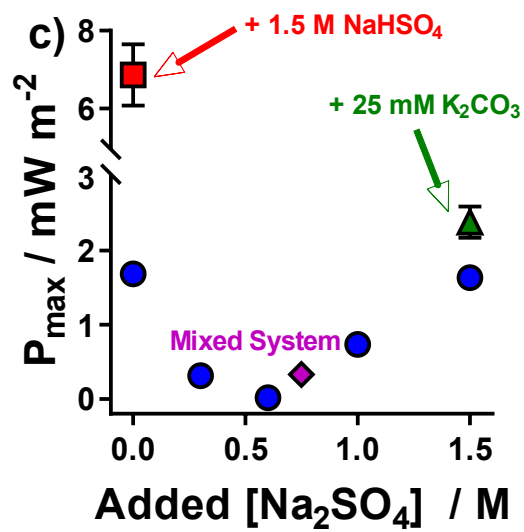


**Figure S12** – (a) Figure 1 and (b, c) Figure 2 from the main manuscript – all adapted to include the mixed thermocell, which comprised 0.3 M  $\text{Fe(II)SO}_4$ , 0.3 M  $\text{Fe(III)SO}_4$ , 0.75 M  $\text{NaHSO}_4$  and 0.75 M  $\text{Na}_2\text{SO}_4$  (purple diamonds).

## References

- 1 M. Al Maimani, J. J. Black and L. Aldous, *Electrochem. commun.*, 2016, **72**, 181–185.
- 2 P. Yang, K. Liu, Q. Chen, X. Mo, Y. Zhou, S. Li, G. Feng and J. Zhou, *Angew. Chem. Int. Ed.*, 2016, **55**, 12050–12053.
- 3 L. Zhang, T. Kim, N. Li, T. J. Kang, J. Chen, J. M. Pringle, M. Zhang, A. H. Kazim, S. Fang, C. Haines, D. Al-Masri, B. A. Cola, J. M. Razal, J. Di, S. Beirne, D. R. MacFarlane, A. Gonzalez-Martin, S. Mathew, Y. H. Kim, G. Wallace and R. H. Baughman, *Adv. Mater.*, 2017, **29**, 1605652.
- 4 J. H. Kim, J. H. Lee, R. R. Palem, M. S. Suh, H. H. Lee and T. J. Kang, *Sci. Rep.*, 2019, **9**, 8706.
- 5 K. Kim, S. Hwang and H. Lee, *Electrochim. Acta*, 2020, **335**, 135651.
- 6 M. A. Buckingham, F. Marken and L. Aldous, *Sustain. Energy Fuels*, 2018, **2**, 2717–2726.
- 7 M. A. Buckingham and L. Aldous, *J. Electroanal. Chem.*, , DOI:10.1016/j.jelechem.2020.114280.
- 8 J. T. Hupp and M. J. Weaver, *J. Phys. Chem.*, 1984, **88**, 1860–1864.
- 9 B. Burrows, *J. Electrochem. Soc.*, 1976, **123**, 154–159.
- 10 J. T. Hupp and M. J. Weaver, *Inorg. Chem.*, 1984, **23**, 3639–3644.
- 11 C. E. Housecroft and A. G. Sharpe, *Inorganic Chemistry*, Pearson Education Limited, 4th Editio., 2012.
- 12 Y. Marcus, *Chem. Rev.*, 1988, **88**, 1475–1498.
- 13 J. S. Murray and P. Politzer, *Croat. Chem. Acta*, 2009, **82**, 267–275.

14 J. C. Slater, *J. Chem. Phys.*, 1964, **41**, 3199–3204.